Electronic Supplementary Material (ESI) for Nanoscale.
This journal is © The Royal Society of Chemistry 2020

Electronic Supplementary Information

AgPd Nanoparticles for Electrocatalytic CO_2 Reduction: Bimetallic Composition-Dependent Ligand and Ensemble Effects

Meiyang Cui,[a] Grayson Johnson,[a] Zhiyong Zhang,[a] Shuang Li,[b] Sooyeon Hwang,[b] Xu Zhang,[c] Sen Zhang*, [a]

[a] Department of Chemistry, University of Virginia, Charlottesville, VA 22904, United States;

[b] Center for Functional Nanomaterials, Brookhaven National Laboratory, Upton, New York 11973, United States;

[c] Department of Physics and Astronomy, California State University Northridge, Northridge, California 91330, United States.

*To whom correspondence should be addressed.

E-mail for S. Z.: sz3t@virginia.edu

Contents:

This file includes Supplement Table S1-S4 and Supplement Figure S1-S18

Table S1. The composition and metal loading of C-AgPd catalysts determined by ICP-OES.

Catalyst	Ag:Pd molar ratio	metal loading wt%	
		Ag	Pd
Ag	100:0	15.6	0
$Ag_{45}Pd_{55}$	45:55	11.2	13.7
$Ag_{37}Pd_{63}$	37:63	8.3	14.7
$Ag_{15}Pd_{85}$	15:85	2.7	15.3
Ag_5Pd_{95}	5:95	1.2	25.1
Pd	0:100	0	26

Table S2. XPS peak assignment and position of AgPd, Pd, and Ag NPs.

Sample	Binding Energy eV			
	Pd $3d_{3/2}$	**Pd $3d_{5/2}$**	**Ag $3d_{3/2}$**	**Ag $3d_{5/2}$**
Pd	341.3	336.0		
$Ag_{15}Pd_{85}$	341.2	335.9	374.1	368.1
$Ag_{37}Pd_{63}$	340.9	335.6	374.1	368.1
$Ag_{45}Pd_{55}$	340.9	335.6	374.2	368.2
Ag			374.8	368.8

Table S3. Faradic efficiency towards formate product and current density on C-Pd catalyst at -0.4 and -0.5 V.

Potential	$FE_{formate}$	Current Density
V vs. RHE	%	mA cm^{-2}
-0.4	93.2	0.15
-0.5	89.5	0.37

Table S4. Peak position of CO_{ads} over Pd and AgPd NPs in DRIFTs spectra at room temperature.

Sample	CO wavenumber cm^{-1}	
	CO_{atop}	$CO_{bridge/hollow}$
Pd	2078.6	1945.8
$Ag_{45}Pd_{55}$	2024.9	1917.7
$Ag_{37}Pd_{63}$	2032.2	1914.5
$Ag_{15}Pd_{85}$	2054.8	1908.3

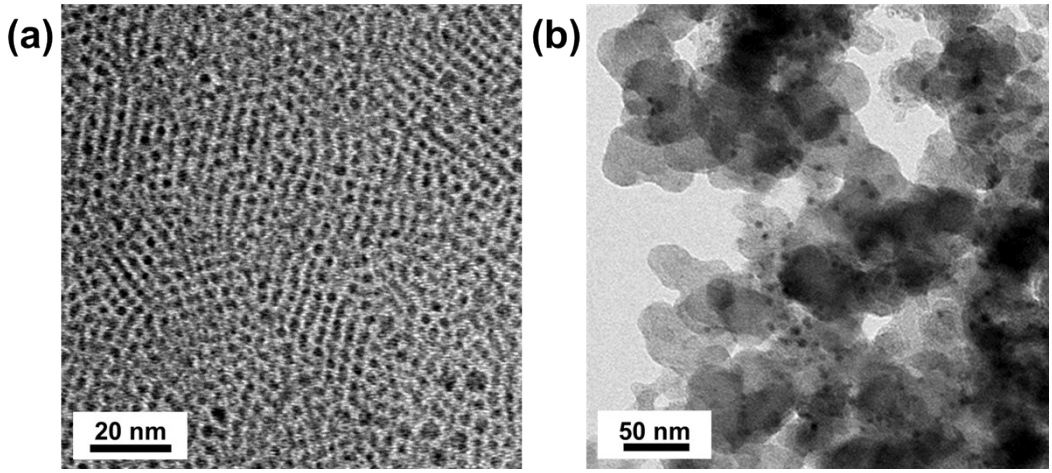

Figure S1. TEM images of (a) as-synthesized Ag NPs and (b) C-Ag after surfactant removal.

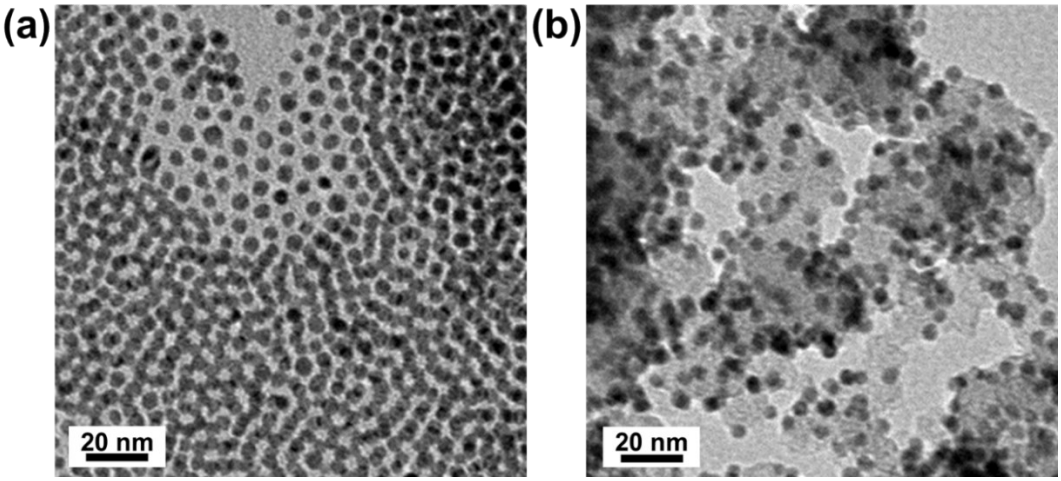

Figure S2. TEM images of (a) as-synthesized Pd NPs and (b) C-Pd after surfactant removal.

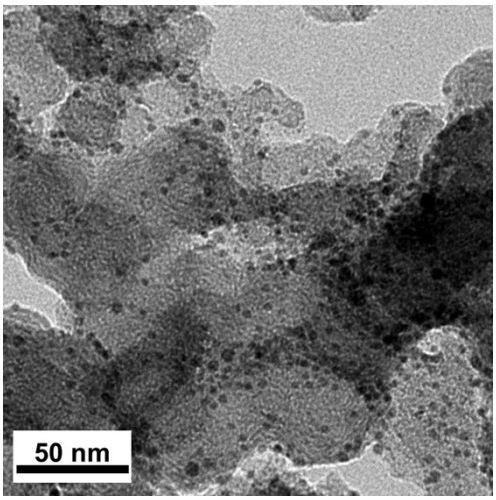

Figure S3. TEM image of C-$Ag_{15}Pd_{85}$ after surfactant removal.

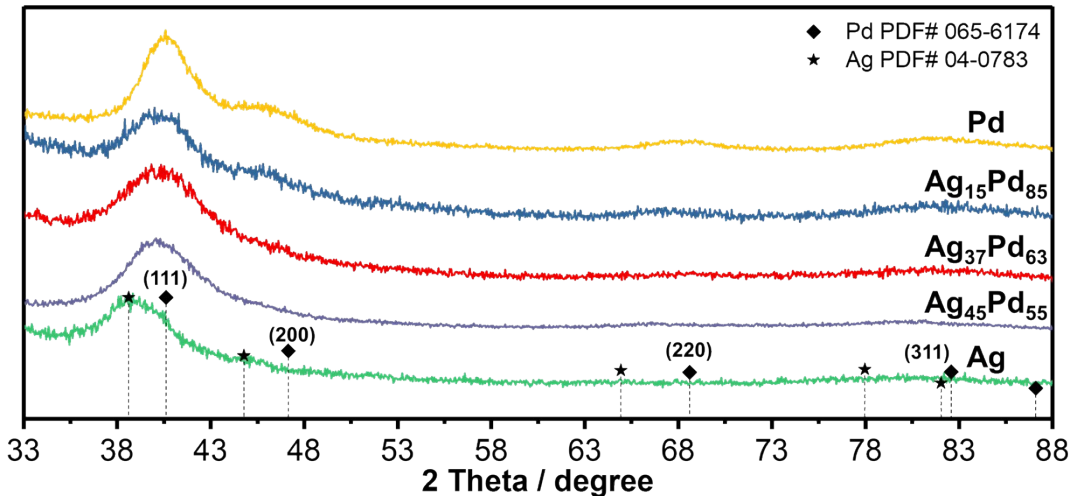

Figure S4. XRD patterns of Ag NPs, Pd NPs and AgPd NPs with different bimetallic ratios.

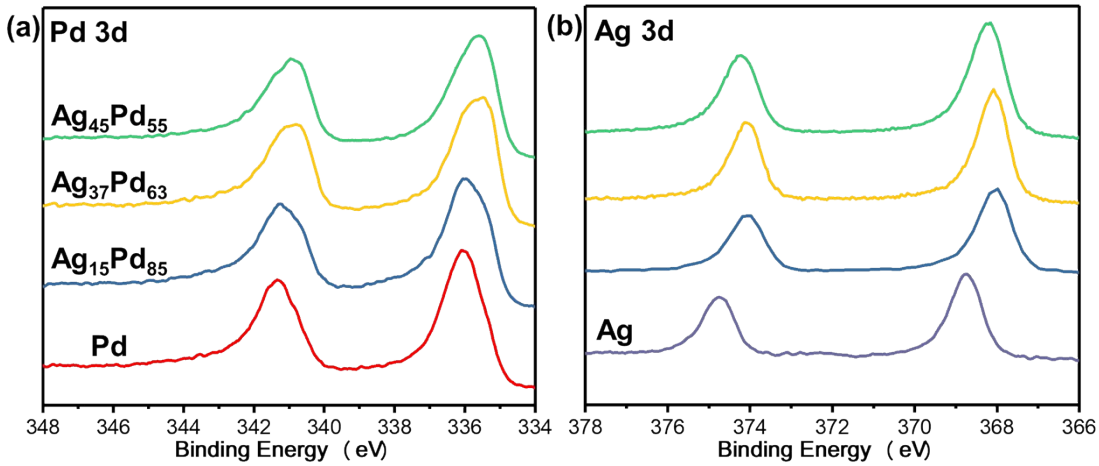

Figure S5. High resolution (a) Pd 3d and (b) Ag 3d XPS spectra of AgPd, Pd and Ag NPs.

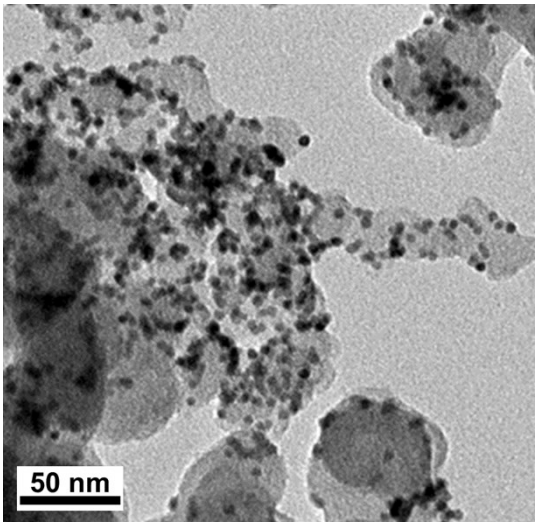

Figure S6. TEM image of C-Pd after a 2-hour electrocatalysis test at -0.8 V.

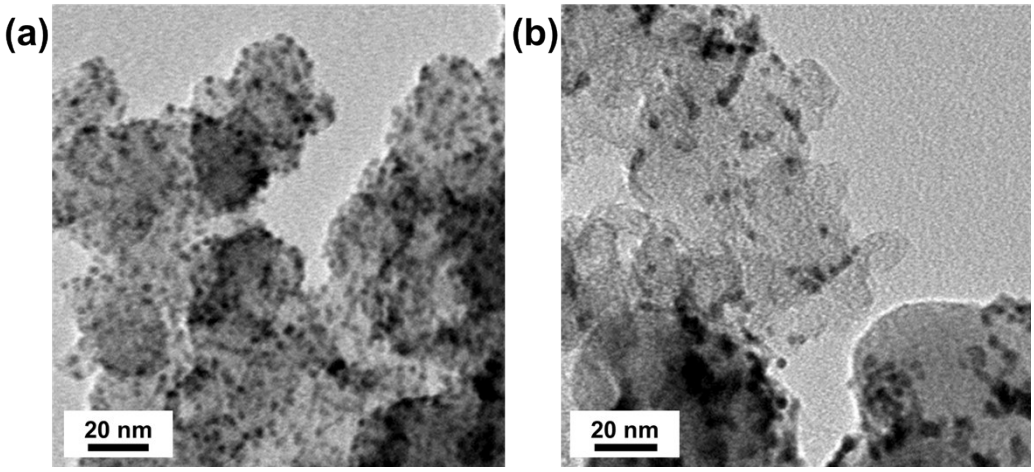

Figure S7. TEM images of C-$Ag_{15}Pd_{85}$ after (a) a 2-hour electrocatalysis test and (b) a 12-hour stability test at -0.8 V.

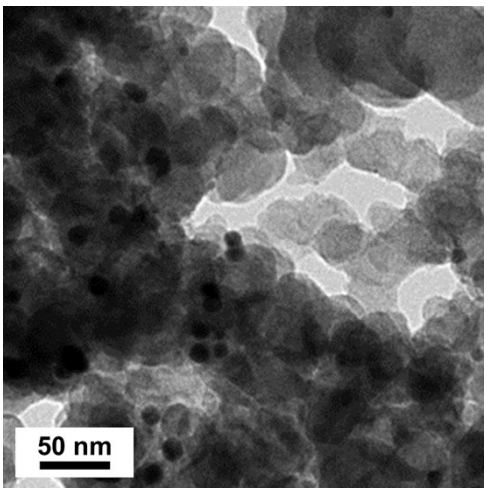

Figure S8. TEM image of C-Ag after a 2-hour electrocatalysis test at -0.8 V.

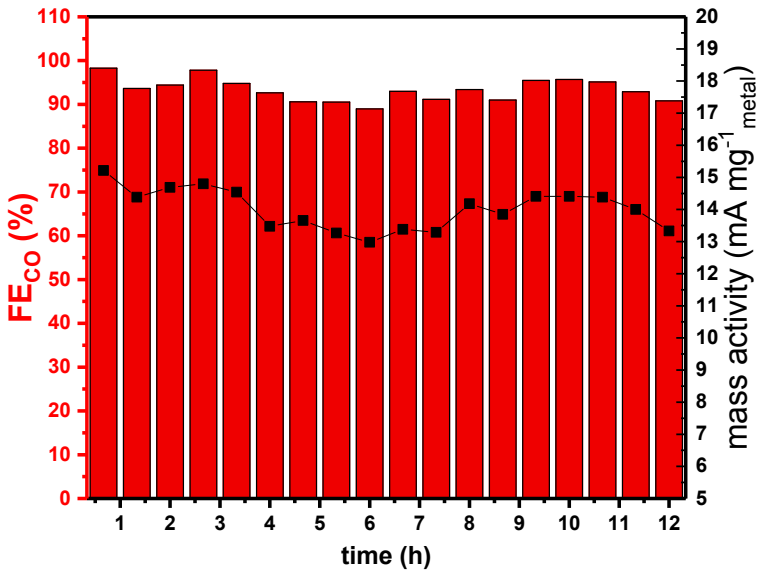

Figure S9. FE_{CO} and mass activity evolution over C-$Ag_{15}Pd_{85}$ during a 12-hour stability test at -0.8 V.

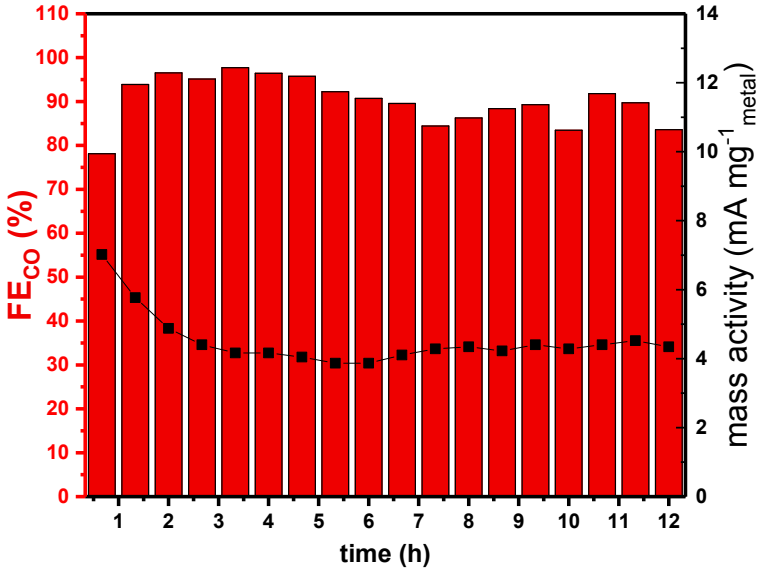

Figure S10. FE_{CO} and mass activity evolution over C-Pd during a 12-hour stability test at -0.8 V.

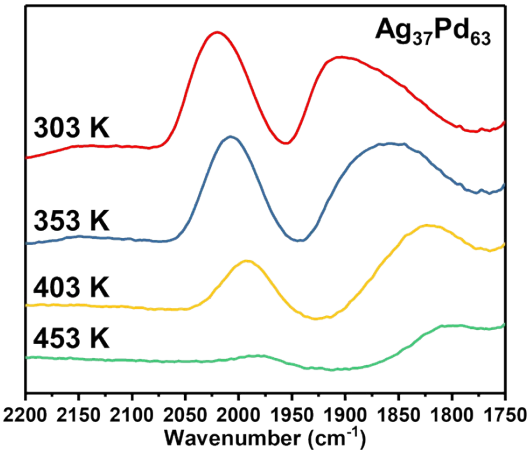

Figure S11. TPD-DRIFTS spectra of alumina-supported $Ag_{37}Pd_{63}$ at 303 K, 353 K, 403 K, and 453 K, respectively.

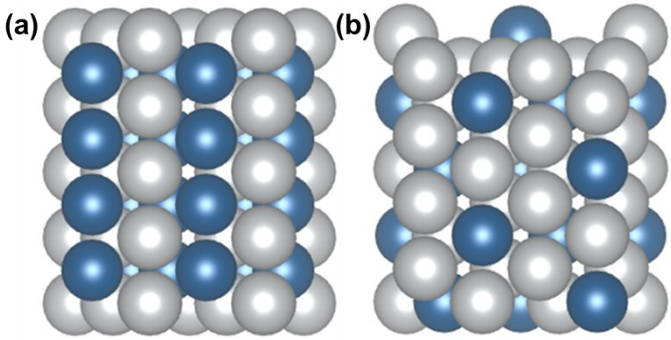

Figure S12. (a) $Ag_{50}Pd_{50}$ (111) surface as generated from the bulk material, (b) Ag_{75} Pd_{25} (111) surface as generated from the bulk. Atom color code: Ag: silver and Pd: blue.

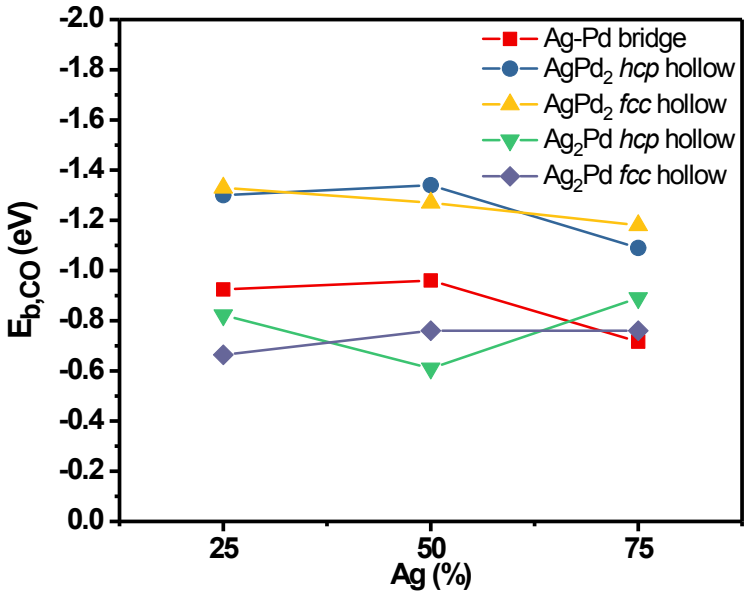

Figure S13. CO adsorption energy on mixed Ag-Pd adsorption sites. All of these adsorption energies are weaker than those of the adjacent Pd only sites reported in Figure 5(e).

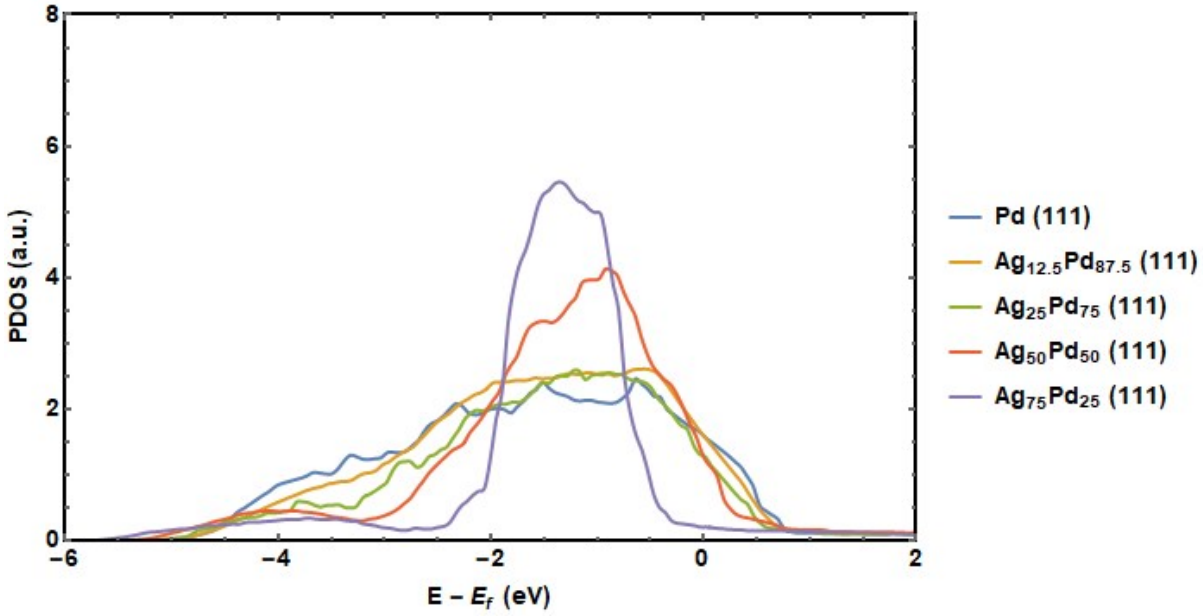

Figure S14. Calculated d-orbital partial density of state (PDOS) of Pd atoms on Pd and AgPd alloy surfaces. The calculated d-band centers are -1.67 eV, -1.57 eV, -1.53 eV, -1.39 eV, and -1.51 eV for Pd, $Ag_{12.5}Pd_{87.5}$, $Ag_{50}Pd_{50}$, and $Ag_{75}Pd_{25}$ respectively.

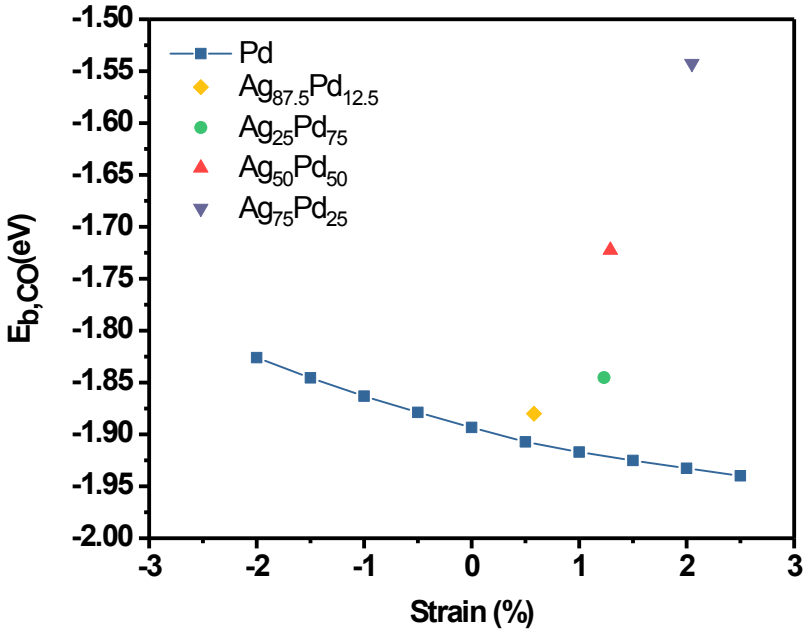

Figure S15. Calculated binding energy of CO in the *fcc* hollow site as a function of strain on the Pd (111) surface was calculated from -2 to 2.5%. The calculated strain of the 3-fold Pd ensembles for the relaxed alloys structures was recorded and the binding energy was compared against that of the pure Pd system. In this type of analysis, points that vary from the artificially strained calculations have contributions from the ligand effects, while points falling along the line have contributions solely from the strain.

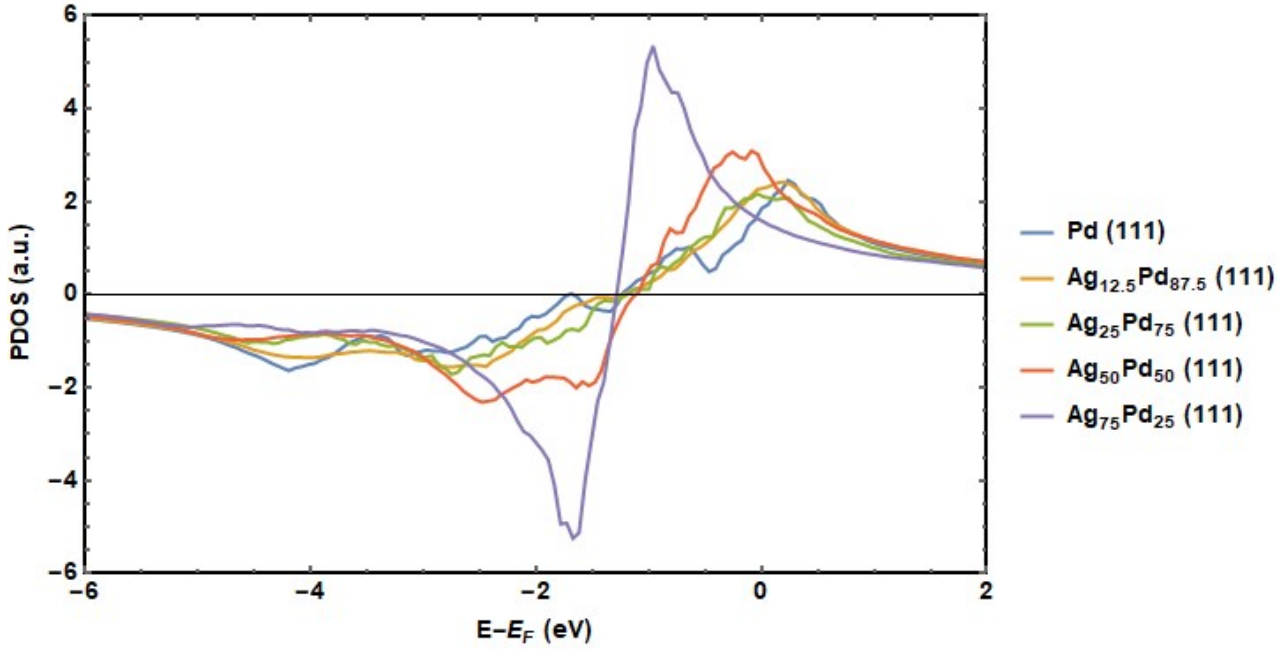

Figure S16. Hilbert transform of the Pd d-PDOS. The energy at which the max of this plot occurs correlates with binding energy in that the further below the Fermi energy it is, the lower in energy the antibonding orbital is, and the weaker the binding energy is.

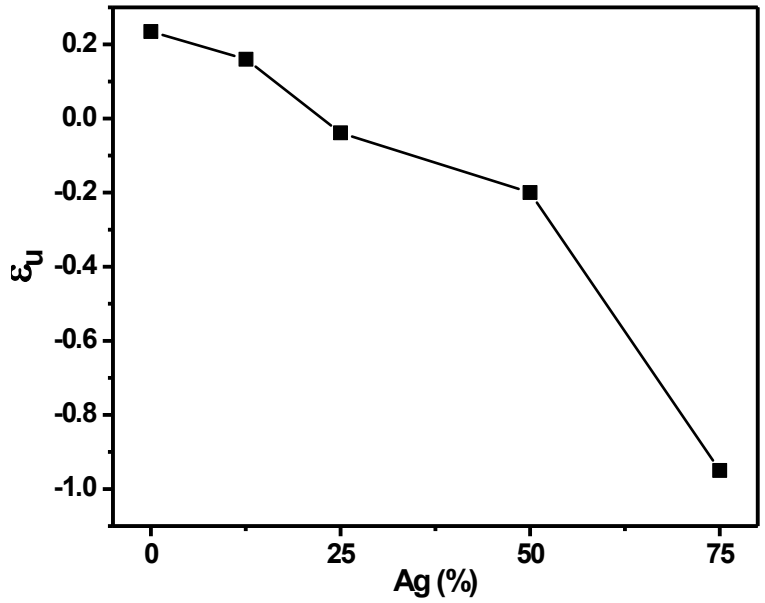

Figure S17. $\varepsilon_{u,}$ from figure the max of figure S16 for each model. This value rapidly changes after 50% Ag addition.

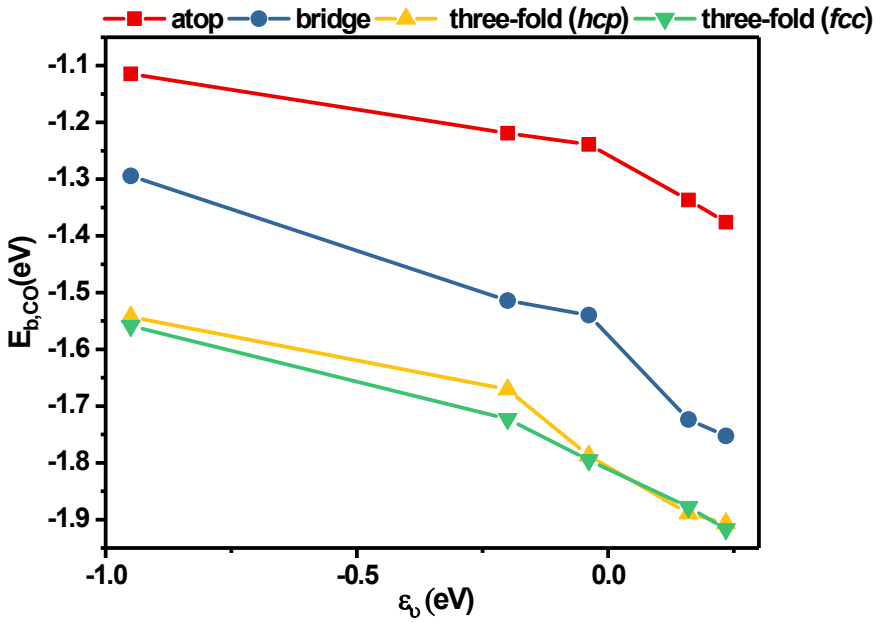

Figure S18. CO binding energy ($E_{b,CO}$) shown as a function of ε_u. As expected by the Anderson – Newns theory of binding, the binding energy is reduced as ε_u falls.